Computer Methods and Programs in Biomedicine 260 (2025) 108529



Contents lists available at ScienceDirect

Computer Methods and Programs in Biomedicine

journal homepage: https://www.sciencedirect.com/journal/computer-methods-and-programs-in-biomedicine





Real-time ultrasound shear wave elastography using a local phase gradient

Enrique González-Mateo, Francisco Camarena, Noé Jiménez *

Instituto de Instrumentación para Imagen Molecular, Universitat Politècnica de València - CSIC, Camino de Vera s/n, 46022, València, Spain

ARTICLE INFO

Keywords:
Ultrasound elastography
Shear wave imaging
Directional filtering
Phase gradient

ABSTRACT

Background and Objective: Current approaches for ultrasound spectral elastography make use of block processing, resulting in long computational times. This work describes a real-time, robust, and quantitative imaging modality to map the elastic and viscoelastic properties of soft tissues using ultrasound.
Methods: This elastographic technique relies on the spectral estimation of the shear-wave phase speed by combining a local phase-gradient method and angular filtering. We first apply directional filtering in the spatio-temporal frequency domain for providing one-way, smooth, and harmonic displacement maps in the frequency range of interest. Thanks to this, we can apply a simple, fast, and local phase gradient approach to obtain the axial and lateral components of the wavevector, which are linked to phase velocity and soft-tissue elasticity and viscoelasticity. The technique is validated numerically and experimentally using a 7.6 MHz ultrasound probe, tested in calibrated soft-tissue phantoms and *ex vivo* liver tissues. The method is compared with state-of-the-art spectral methods.
Results: The technique significantly reduces the computation time, e.g., the reconstruction time for a 155 × 315-pixel phase-velocity map was 0.16 s, while local-phase velocity-imaging techniques was 156.73 s for 2D implementation and 13.56 s for the 1D version, a reduction between two and three orders of magnitude, while showing a similar accuracy and resolution than standard methods.
Conclusions: This approach eliminates the need for block processing that may limit the spatial resolution and computational time of the velocity map. In this way, the phase gradient elastography method is revealed as an efficient and robust approach for real-time spectral elastography.

1. Introduction

Ultrasound imaging produces morphological images by mapping tissue echogenicity, i.e., its ability to scatter acoustic waves [1]. However, tissues with different stiffness can present similar acoustic reflectivity, appearing with similar gray-level speckle in classical B-mode ultrasound images. To enhance ultrasound sensitivity and specificity, elastography has emerged as a reliable medical diagnostic tool, mapping and quantifying soft tissue elasticity, where local stiffness has been identified as a reliable biomarker linked to several pathologies [2]. Ultrasound elastography combines standard ultrasound imaging with a source of mechanical vibration, endogenous [3] or exogenous [4], to measure tissue stiffness by quantifying the degree of tissue strain or displacement in response to the stress [5]. This technology is a safe, portable, and cost-effective alternative to other imaging techniques, such as MRI or CT scans, which require expensive equipment and/or radiation exposure.

The earliest techniques of ultrasound elastography were based on the measurement of the degree of deformation experienced by a tissue because of the application of a constant stress, which could be externally applied, for example, through palpation, or internally, as in the case of respiration or the heartbeat. These quasi-static methods provide images of relative strain [6], but the absolute tissue stiffness remains unknown [7]. Additionally, information on properties like viscoelasticity [8] is typically not provided by these quasi-static methods. More advanced techniques as dynamic methods measure the deformation induced by a time-varying force, it can either be a short transient mechanical force or an oscillatory force with a fixed frequency. Transient acoustic radiation force can produce deformations deep into tissue, generating transversely propagating shear waves, whose speed is linked to the shear stiffness of the tissue. In this way, Shear Wave Elastography Imaging [9] or Supersonic Shear Wave imaging [10], between other modalities, can quantitatively map tissue shear stiffness in a quantitative way. Shear waves can also be generated by external vibrating sources, like in the case of transient elastography [11].

Dynamic techniques can provide insights into the mechanical properties of soft tissues, including elasticity, viscosity, and mechanical

* Corresponding author.
E-mail address: nojigon@upv.es (N. Jiménez).

https://doi.org/10.1016/j.cmpb.2024.108529
Received 29 July 2024; Received in revised form 18 November 2024; Accepted 24 November 2024
Available online 29 November 2024
0169-2607/© 2024 The Authors. Published by Elsevier B.V. This is an open access article under the CC BY license (http://creativecommons.org/licenses/by/4.0/).

impedance. However, a spectral analysis of the phase-velocity dispersion of the shear-wave is usually required for this purpose [8], offering a more thorough insight into the mechanical properties of tissue. Indeed, this information is useful in terms of identifying new biomarkers for a more accurate medical diagnosis [12–14].

In this context, it becomes critical to distinguish between two ways for calculating shear wave velocity: time-domain methods based on time of flight (TOF) estimations [15,16], and frequency-domain methods that use phase-based approaches [17–19] or spectral processing [20–22]. Time-of-flight methods measure the shear-wave transit time between two points to estimate its group velocity, whereas frequency-domain methods estimate phase velocity by analyzing the spectrum of the shear wave displacement map. Most time-domain techniques do not consider viscoelasticity because they rely on average group velocity, assuming a linear, elastic, and isotropic tissue. In contrast, spectral methods can estimate the phase velocity as a function of the frequency, i.e., the dispersion curves, and can provide the viscoelastic parameters. In addition, spectral methods have been recently proposed to retrieve other properties like anisotropy [23] or non-linearity [24].

There are real-time elasticity image mapping implementation approaches [25], although they are primarily time-domain based. The challenge with employing spectral algorithms for soft-tissue mapping is that the spatio-temporal transforms and involved processing, e.g., Fourier transforms combined with block processing, have a significant computational cost [21] and, even when using parallelized GPU processing, may render real-time reconstruction of multiple phase-velocity images unaffordable.

To address these challenges, in this work we propose a real-time shear-wave spectral elastography imaging method. The technique relies on the estimation of the shear-wave phase speed in the frequency domain by using a robust, fast, and local wavevector estimator. To do so, directional filtering in the angular spectrum is exploited first, providing smooth and harmonic displacement maps. Then, by using a fast and local phase gradient approach, the axial and lateral components of the wavevector are obtained, which are ultimately linked to phase speed and soft-tissue elasticity. This phase gradient elastography (PGE) approach eliminates the need for iterative or block processing techniques that limit the spatial resolution of the velocity map when using large block sizes. In this manner, the computational times associated with phase-velocity map reconstruction are significantly reduced, allowing real-time spectral elastography.

To assess the efficacy of the proposed method, a comparative analysis is conducted between phase velocity maps generated by the newly introduced phase-gradient technique and a reference approach, Local Phase Velocity Imaging (LPVI) [20]. The LPVI method calculates the wavenumber in the frequency domain using a recursive two-dimensional fast Fourier transform (LPVI-2D). Additionally, an optimized variant of the LPVI method is considered, which employs a one-dimensional fast Fourier transform (LPVI-1D) while adhering to the same underlying principles [21]. The computational complexity of the three methods is evaluated by comparing their respective computation times. The performance of the proposed technique is further assessed through 3D full-wave simulations in incompressible viscoelastic media. Experimental validation is carried out using soft-tissue phantoms and an *ex vivo* bovine liver tissue sample, demonstrating the method's applicability in a more realistic scenario.

2. Methods

2.1. Phase gradient elastography method

We start assuming a shear wave has been generated inside a soft tissue using the acoustic radiation force of a focused ultrasound beam, and a set of fast B-mode acquisitions were performed to track the resulting tissue displacements, as usually in most shear wave elastography modalities. Fig. 1 summarizes the algorithm's operating scheme, divided into four main steps.

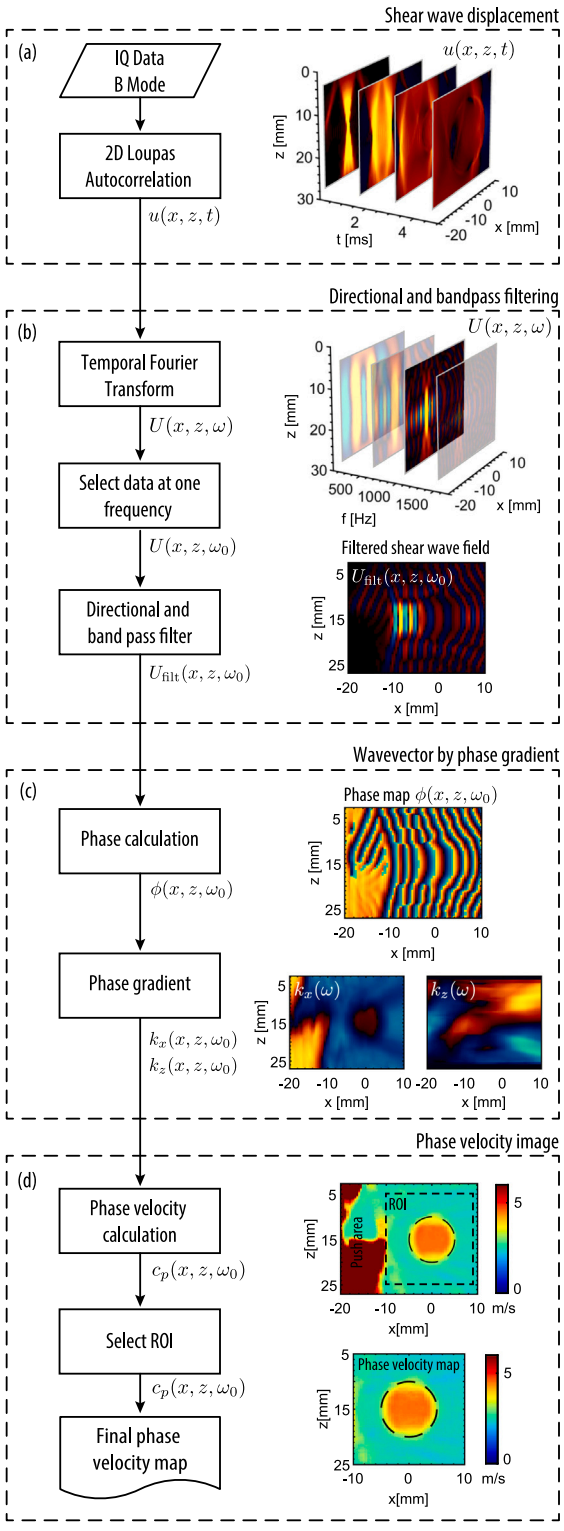


Fig. 1. Flowchart of phase gradient elastography (PGE) method. (a) Shear-wave displacements are tracked. (b) Wavenumber and directional filter are applied. (c) Wavenumber components are retrieved using a phase gradient approach. (d) Phase velocity map is reconstructed within a region of interest.

2.1.1. Shear wave particle velocity estimation

The input data for estimating tissue deformation consists of a set of $n = 1, 2, \ldots, N$ pixel-based in-phase (I) and quadrature (Q) frames, $IQ(x, z, t)$, where x and z are the spatial coordinates and $t = n/f_s$,

where $f_s = \omega/2\pi$ is the slow-time sampling frequency, i.e., the ultrasound imaging frame rate, and ω the corresponding angular frequency, Fig. 1(a). The z component of the tissue velocity field, $u_z(x,z,t)$, is estimated by using a 2D autocorrelator [26]. This estimator gives the particle velocity by calculating the mean Doppler frequency, by measuring the I and Q components of the reflected pulsed signals at different time frames. This autocorrelation can be implemented as a convolution in the depth and time directions. For this, it is necessary to have a window of depth samples and a few pulse transmissions, respectively, which are used to derive an axial velocity estimate. The results of the phase velocity map reconstruction depend on these two factors. The number of samples in depth must adhere to a standard because smoother displacements result from more samples in depth. The 2D autocorrelator can attain superior precision for a depth gate of 3 wavelengths [27]. On the other hand, the number of samples in time, or the duration of the number of tracking pulses, must not exceed one period of the frequency under consideration. If we increase this value, we will be averaging temporal shifts while losing frequency-domain information.

2.1.2. Temporal, angular and bandpass filtering

In practice, the presence of reflected waves or non-flat shear-wave wavefronts can prevent the direct reconstruction of phase velocity images [28]. In addition, phase gradient methods can be sensitive to noise and artifacts in the data, which can lead to errors in the estimation of phase velocity [17]. Utilizing bandpass filters enhances the reconstruction process of phase velocity maps, thereby expanding the frequency spectrum within which these maps can be accurately reconstructed [22]. Therefore, we make use of wavenumber [29] to limit the values of phase velocity within typical ranges, and directional filters [30,31] to eliminate reflected waves and multiple scattering, by narrowing the angular spectrum of the tissue motion, Fig. 1(b).

The implementation is performed in the spatio-temporal frequency domain. First, the tissue motion spectrum, $U(x,z,\omega)$, is calculated by a 1D Fourier transform in the temporal direction,

$$U(x,z,\omega) = \mathcal{F}_t[u_z(x,z,t)], \tag{1}$$

using a N_t-point Fast Fourier Transform (FFT) algorithm, where $N_t = 2^n$, and n is the exponent for the smallest power of two that satisfy $2^n \geq N$. The bandwidth of interest in shear wave motion is determined by locating the peak energy within its $k-\omega$ spectrum. In this study, the lower cut-off frequency is typically selected at the point where the spectrum decreases by 3 dB, denoted as $\omega_{-3\text{ dB}}$, relative to the center frequency. Conversely, the upper cut-off frequency is identified where the spectrum decreases by 6 to 12 dB, represented as $\omega_{-6\text{ dB}}$ and $\omega_{-12\text{ dB}}$, contingent on the medium's attenuation characteristics. Within this bandwidth, a set of interest frequencies, ω_0, were selected. Note a lower cut-off frequency was not used because this large-wavelength range does not provide relevant spatial information and its spectrum presents a low energy level [32]. Once the motion field at each interest frequency has been chosen, it is transformed to the frequency–wavenumber domain $U(k_x,k_z,\omega_0)$ by means of a 2D spatial Fourier transform,

$$U(k_x,k_z,\omega_0) = \mathcal{F}_k[U(x,z,\omega_0)], \tag{2}$$

performed using a $N_x \times N_z$-points 2D-FFT algorithm, where k_x and k_z are the components if the wavevector in the $x-z$ directions, respectively.

The spatial filtering is implemented by directional and band-pass filters. The spectral magnitude of the three Gaussian filters, designed in polar coordinates in the k-space, is given by

$$G_\varphi(\varphi) = \exp\left[-\frac{1}{2}\left(\frac{\varphi-\bar{\varphi}}{\Delta\varphi}\right)^2\right], \tag{3}$$

$$G_r(k_r) = \exp\left[-\frac{1}{2}\left(\frac{k_r-\bar{k}_r}{\Delta k_r}\right)^2\right], \tag{4}$$

$$G_0(k_r) = 1-\exp\left[-\frac{1}{2}\left(\frac{k_r}{\Delta k_0}\right)^2\right], \tag{5}$$

where $\varphi = \arctan(k_z/k_x)$ denotes the polar angle, and $k_r^2 = k_x^2 + k_z^2$ represents the radial component. In Eq. (3), the directional filter's central direction ($\bar{\varphi}$) and angular bandwidth ($\Delta\varphi$) are crucial parameters. While smaller $\Delta\varphi$ values result in flatter wavefronts, ideal for homogeneous media, excessively narrow angular bandwidths may lead to spatial information loss and phase velocity overestimation during object reconstruction. Therefore, intermediate bandwidths are recommended for optimal performance. On the one hand, note that for the phase-gradient to work, we cannot have counter-propagating modes in any direction, including the transverse. Therefore, the theoretical upper bound for the bandwidth is $\pi/2$. On the other hand, extremely narrow filters result in a loose of resolution of the resulting image in the transverse direction of the filter direction, especially in heterogeneous media. Numerical tests show that these parameters may be within the range $\pi/8 \leq \Delta\varphi \leq \pi/4$. A parametric study to show the shape of the filtered wavefront as a function of the width of the directional filter is given in the Supplementary Material 1. In Eq. (4), the wavenumber filter is defined by $\bar{k}_r = (k_{\max}+k_{\min})/2$ and $\Delta k_r = k_{\max}-k_{\min}$ which are the central wavenumber and angular spectrum bandwidth of the bandpass filter, respectively, given by the phase velocity limits $k_{\min} = \omega/c_{\max}$ and $k_{\max} = \omega/c_{\min}$. In homogeneous media, we first obtain the mean phase velocity $c_{\mathcal{F}_{2D}}$ using the two-dimensional Fourier transform (2D-FT) method [33] at the central frequency and, then, the phase velocity range is given by $c_{\min} = c_{\mathcal{F}_{2D}} - c_k$ m/s and $c_{\max} = c_{\mathcal{F}_{2D}} + c_k$ m/s, with c_k set at 0.5 m/s empirically [22]. Conversely, in heterogeneous media, the filter bandwidth spans from 0.5 to 11.0 m/s, corresponding to typical shear wave velocity values in soft tissues. Lastly, in Eq. (5), the parameter Δk_0 is the DC filter bandwidth, set to $k_{\min}/8$ to attenuate zero-frequency modes. Then, using Eqs. (3)–(5), the filtered motion is obtained as

$$U_{\text{filt}}(k_x,k_z,\omega_0) = U(k_x,k_z,\omega_0)\cdot G_\varphi \cdot G_r \cdot G_0. \tag{6}$$

Finally, the filtered data is converted to the space-frequency domain $U_{\text{filt}}(x,z,\omega_0)$ using a 2D inverse Fourier transform as

$$U_{\text{filt}}\left(x,z,\omega_0\right) = \mathcal{F}_k^{-1}\left[U_{\text{filt}}\left(k_x,k_z,\omega_0\right)\right], \tag{7}$$

by using a $N_x \times N_z$-points inverse 2D-FFT algorithm.

2.1.3. Wavenumber calculation using a phase gradient

If we consider a plane shear wave traveling in a direction given by elevation and azimuth angles (θ, φ), with a wavevector $\mathbf{k}$, the components of the wavevector can be defined for convenience as $k_x = k\sin\varphi\sin\theta$, $k_z = k\cos\varphi\sin\theta$, and $k_y = k\sin\theta$, where $k^2 = k_x^2 + k_z^2 + k_y^2$. Assuming a plane harmonic wave propagating in the $\theta = 0$ direction, then $k_y = 0$. Therefore, the amplitude of the shear wave reduces to

$$U(x,z,\omega_0) = U_0\exp\left[-i\phi(x,z)\right], \tag{8}$$

where a time dependence of $\exp(i\omega t)$ is assumed, U_0 is the wave amplitude and $\phi(x,z) = \left(k_x x + k_z z\right)$ gives the local phase distribution. Therefore, we can simply obtain the components of the wavevector, k_x and k_z, by calculating the gradient of the phase of the plane wave, $\nabla\arg(U)$, as

$$\nabla\arg\left[U(x,z,\omega_0)\right] = \nabla\phi(x,z) = k_x\hat{x} + k_z\hat{z} = \mathbf{k}, \tag{9}$$

where $\hat{x}$ and $\hat{z}$ are the unitary vectors. Usually, the components of the wavevector cannot be calculated using this straightforward approach because it becomes cumbersome to experimentally generate a harmonic plane wave traveling through the image plane ($y = 0$). By pushing the tissue using an acoustic radiation force, the generated shear wave generally presents a broad and complex angular spectrum due to, e.g., initial conditions, reflections or refraction, including wavefront replicas in multiple directions. Therefore, Eq. (9) does not generally provide the wavevector.

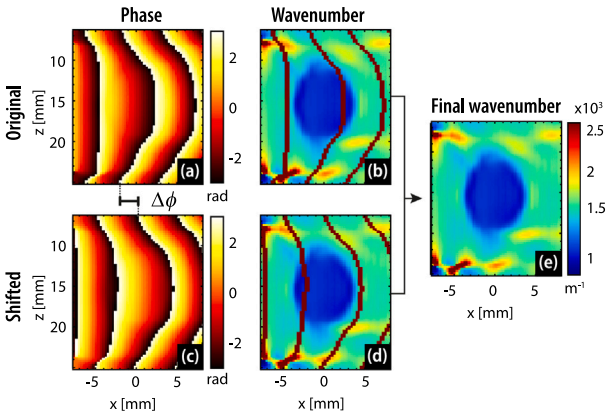


Fig. 2. Phase (a) (c) and wavenumber (b) (d) of the original and the shifted shear wave motion data. The data is shifted $\Delta\phi$ radians to estimate the spatial wavenumber avoiding phase discontinuities. The final wavenumber map (e) is compounded by original and shifted wavenumber maps.

However, the key of the current approach is the directional and band-pass filtering, which enables a plane-wave decomposition of the tissue motion. Using the filters, the resulting motion, $U_{\text{filt}}\left(x, z, \omega_0\right)$, takes the form of Eq. (8) and, then, the assumptions to apply Eq. (9) are fulfilled.

The discontinuities in the phase map due to phase jumps must be avoided to calculate the gradient, see Fig. 2(b,d). Numerical tests have shown that the phase gradient slope is strongly sensitive to the small artifacts introduced by existing phase unwrapping methods. Therefore, in this work the computation of the wavenumber is carried out in three steps. First, by using a second-order accuracy centered finite-difference approximation [34] the wavevector components are calculated from the wrapped phase map, which includes discontinuities. Second, the process is repeated by using a π-shifted version of the wrapped phase map, also including discontinuities. Third, phase discontinuities are identified by using a threshold on both phase maps, and two binary masks are designed. Finally, the masks are used to merge both wavevector components into a smooth map of the final wavenumber, as shown in Fig. 2(e). Note that, both original and π-shifted versions of the phase map, may present jumps near phase dislocations. At these particular pixels, images cannot be composed for this frequency because the gradient is not defined. However, a nearby frequency provides information at these points and, therefore, can be used to compose a smooth image.

2.1.4. Phase velocity map

Once the wavevector is calculated, the phase velocity image, for each spectral component ω_0, is given by

$$c_{\text{ph}}(x, z, \omega_0) = \frac{\omega_0}{\sqrt{k_x^2(x, z, \omega_0) + k_z^2(x, z, \omega_0)}}. \tag{10}$$

Finally, a region of interest (ROI) is selected. The ROI is placed on one side of the push beam focus, matching the orientation of the directional filters used. While this algorithm provides the phase velocity map for a given frequency, it is possible to average images in a bandwidth around the shear wave central frequency to compose an average shear wave phase velocity image, Fig. 1(d). Indeed, this process removes eventual artifacts due to phase dislocations.

To demonstrate and evaluate the performance of the proposed approach, the technique was implemented in MATLAB (MathWorks, Natick, MA, USA) on a standalone computer running Windows 11 Professional and a CPU Intel(R) Core (TM) i9-10900F CPU at 2.80 GHz and 32 GB RAM.

2.2. Simulation experiment

In addition to the experiments, we simulate a L11-5v phased array probe (Verasonics Inc., Redmond, WA) using the simulation method described in Appendix A. The probe presents 128 elements, each measuring 0.27 mm in width, 5 mm in height, a kerf of 30 μm, elevation focus of 18 mm, and a central frequency of 7.6 MHz. The push-beam was performed using 32 active channels at a focal depth of 15 mm, resulting in an f-number of 1.74, and the pulse duration corresponds to 200 μs.

Two types of mediums were simulated for shear wave propagation: homogeneous and heterogeneous. In both, the sound speed, density, and longitudinal wave absorption were fixed at 1540 m/s, 1000 kg/m^3, and 0.5 dB/MHz/cm, respectively. For the homogeneous medium, a set of elastic and viscoelastic phantoms are simulated considering a set of Kelvin–Voigt media according to [35]. On the one hand, the elastic phantoms are characterized by a shear elastic modulus (μ_1) varying between 2.25 and 30.25 kPa and a viscoelastic modulus (μ_2) fixed at 0 Pa s. On the other hand, the viscoelastic phantoms are characterized by $\mu_1 = 6.25$ kPa and a viscosity varying between 0 and 2 Pa s. The simulated heterogeneous medium consists of an elastic phantom composed by an 8 mm-diameter spherical inclusion of $\mu_1 = 16$ kPa embedded in a background of $\mu_1 = 4$ kPa. In this case the viscosity was set to $\mu_2 = 0$ Pa s.

Then, the simulated motion data sets were processed using the phase gradient algorithm steps. The bandpass wavenumber filter was characterized with shear wave velocity cut-off of $c_{\min} = c_{\mathcal{F}_{2D}} - c_k$ and $c_{\max} = c_{\mathcal{F}_{2D}} + c_k$ m/s for the homogeneous case, and with $c_{\min} = 0.5$ m/s and $c_{\max} = 11.0$ m/s for the heterogeneous case. Directional filter parameters were fixed at $\Delta\varphi = \pi/4$ and $\bar{\varphi} = 0$ rad, to get the right-traveling wave.

2.3. Phase velocity dispersion curves

Phase velocity dispersion curves were calculated using the phase gradient approach for the simulated homogeneous and heterogeneous cases, as well as for the experimental phantom. Dispersion curves were compared with the two-dimensional Fourier method (2D-FT) [33]. The input data for the 2D-FT method is the shear motion temporal waveforms measured along a lateral line at the depth of the ARF focus. This spatio-temporal information is then transferred to $k-\omega$ space, where the energy peaks are detected and the phase velocity is calculated by a linear fit, using Eq. (10). To obtain a standard deviation for this method, the initial point of the input data was varied between 0 and 4 mm from the focal zone considering a several path lengths. On the other hand, for the phase gradient approach the standard deviation was calculated averaging the reconstructed phase velocity map in ROI near the focal zone with the same axial and lateral length as in the 2D-FT method.

The shear elastic and viscoelastic parameters were calculated by fitting the phase velocity curves to the KV model, see Eq. (A.8). The criterion for choosing the frequency range for the fit is based on finding where most of the energy is in the $k-\omega$ spectrum of the motion wave. The initial value chosen corresponds to the first drop frequency at 3 dB before the center frequency, $\omega_{-3\text{ dB}}$. The final value of the bandwidth in elastic media, where the losses are lower, can be extended to the spectrum drop to 12 dB, $\omega_{-12\text{ dB}}$, but in viscoelastic media the criterion was set to the drop to 6 dB, $\omega_{-6\text{ dB}}$, due to the attenuation of the wave motion by the viscosity.

2.4. Phantom experiment

Experiments were conducted using a CIRS 049 ultrasound elasticity phantom (Computerized Imaging Reference Systems, Norfolk, USA). The phantom is composed of a variety of spherical inclusions of varying size and elasticity, located at different depths embedded

in a homogeneous soft-solid material, all presenting similar ultrasound echogenicity. The Young's modulus of the surrounding material listed in the datasheet is 18 kPa, and it includes four spheres of 6, 9, 36, and 70 kPa. Assuming an incompressible and isotropic elastic material, the following relationship between Young's modulus (E), shear elastic modulus (μ_1) and shear wave velocity can be applied

$$E \approx 3\mu_1 = 3\rho_0 c_s^2, \tag{11}$$

resulting in a shear wave velocity of $c_s = 2.4$ m/s for the background and 1.4, 1.7, 3.5 and 4.8 m/s for the inclusions.

A 128-element L11-5v phased array probe coupled to a Verasonics research equipment (Verasonics Inc., Redmond, WA) was used. The push beam was focused at 15 mm depth, at the left of each inclusion, using 32 active elements using a pulse of 1500 cycles at 7.6 MHz, corresponding with to a length of 200 μs. Tracking pulses for the detection of tissue deformation were emitted at the probe central frequency at a pulse repetition frequency of 10 kHz. The shear wave particle motion was calculated applying the 2D Loupass autocorrelator [26] to the IQ data obtained directly as an output from the Verasonics ultrasound system. Blocks of 12 time samples and 3 wavelengths in depth were used to correlate the displacements. Shear waves between 0.5 and 6.0 m/s were filtered using same filter parameters than in simulation. A final phase velocity image was reconstructed by averaging shear wave maps in a frequency bandwidth near to the central shear wave frequency.

2.5. Ex vivo bovine liver experiment

The imaging technique was validated using *ex vivo* bovine liver tissues. A 10-mm diameter cylindrical inclusion of bovine liver was immersed in a water bath with a 10% concentration of formalin and underwent a vacuum chamber treatment for half an hour to ensure the elimination of trapped air. These preparatory measures were taken to ensure the accuracy and reliability of the experimental setup when validating the method with real tissue samples. In addition, formalin treatment acting on the external layers of the cylindrical liver inclusion modify the elasticity distribution, creating a stiff ring surrounding a soft core, that will be used to test the resolution of the algorithm. Finally, the liver tissue inclusion was embedded in a gelatin phantom, designed to exhibit a shear velocity of 2.5 m/s [36]. *Ex vivo* experiments were carried out using the same procedure and post-processing parameters as in the phantom experiments (Section 2.4).

3. Results

3.1. Simulation validation for homogeneous elastic and viscoelastic media

We start showing the validation of the phase-gradient approach in simulations for a homogeneous elastic medium with $\mu_1 = 6.25$ kPa, $\mu_2 = 0$ Pa s and a viscoelastic medium with $\mu_1 = 6.25$ kPa, $\mu_2 = 1.5$ Pa s, and its comparison with the 2D-FT method. The shear motion waveforms measured along the lateral distance at a depth corresponding to the push focus, for the elastic and viscoelastic materials are shown in Fig. 3(a,g), respectively. Next, the wave-motion is converted to the spatio-temporal frequency domain, $U(k_x, \omega_0)$, resulting in the k-space spectrum maps shown in Fig. 3(b,h). The shear wave frequency spectrum is analyzed to estimate the shear wave frequency bandwidth. In this case, the chosen bandwidth is between the lower −3 dB and the upper −12 dB cut-off frequencies ($\omega_{-3\text{ dB}}$, $\omega_{-12\text{ dB}}$).

Phase velocity dispersion curves, shown in Fig. 3(c,i), obtained with the proposed PGE method are compared with the theoretical KV model and a reference technique using the 2D-FT method [33]. To obtain a local phase velocity by the PGE method at each frequency, a spatial averaging of a ROI close to the focus of the push beam is performed. The ROIs for each case are delineated by a dashed rectangle in the phase velocity maps presented in Fig. 3(d–f, j–l). The PGE error bars correspond to the standard deviation of this average. The standard deviation for the 2D-FT data were calculated averaging the result of processing lateral segments of different lengths. Finally, reconstructed phase velocity maps with the proposed method at different frequencies inside the frequency bandwidth are represented in Fig. 3(d, f) for elastic and Fig. 3(j, l) for the viscoelastic case.

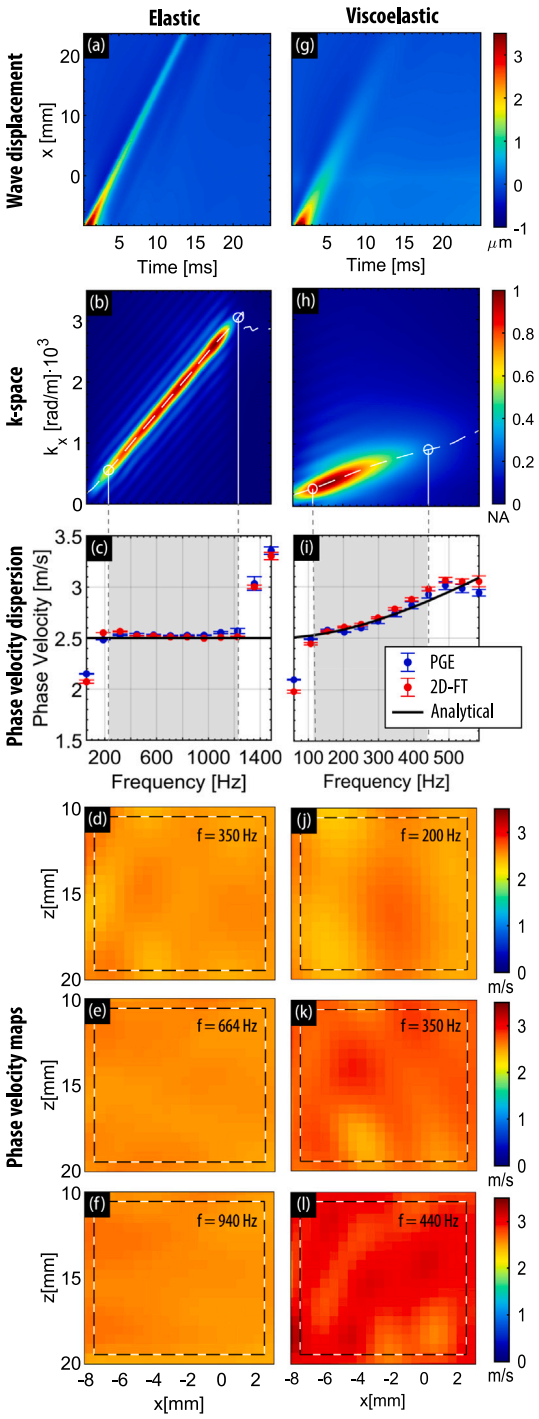


Fig. 3. Phase velocity results for (a–f) an elastic medium and (g–l) a viscoelastic medium with the following parameters: $\mu_1 = 6.25$ kPa, $\mu_2 = 0$ Pa s, and $\mu_1 = 6.25$ kPa, $\mu_2 = 1.50$ Pa s, respectively. The (a,g) wave motion in the space–time domain. (b,h) spatio-temporal wave motion spectrum. (c,i) phase velocity dispersion obtained with (black) the KV analytical model, (red) the 2D-FT method, and (blue) the PGE approach, the gray shaded area indicates the bandwidth. (d–f) phase velocity maps for different frequencies for the elastic and (j–l) viscoelastic phantom.

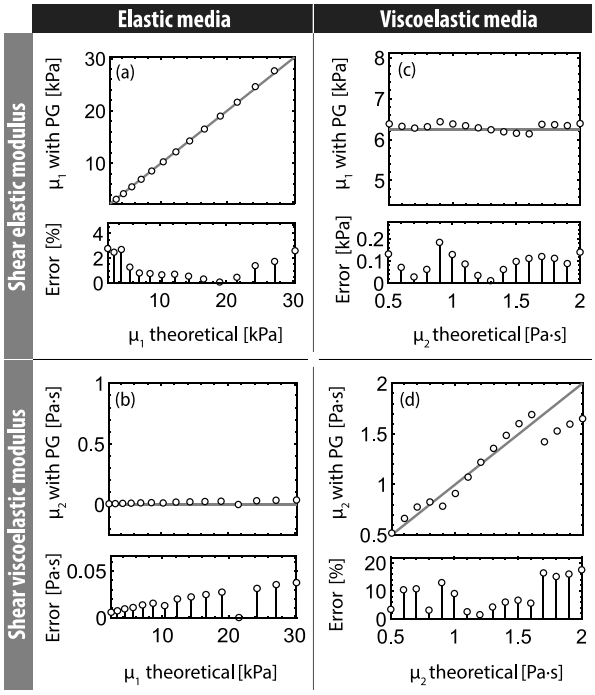


Fig. 4. Characterization of the elastic and viscoelastic homogeneous media using simulations. Each point corresponds to a different phantom. (a) Retrieved shear elastic and (b) viscoelastic moduli versus theoretical values, shear elastic modulus was in the range $2.25 < \mu_1 < 30.25$ kPa, viscosity is fixed to $\mu_2 = 0$ Pa s. (c) Retrieved shear elastic and (d) viscoelastic modulus, elastic modulus was set to $\mu_1 = 6.25$ kPa and viscosity was in the range $0 < \mu_2 < 2$ Pa s. The continuous gray line represents the theoretical values, while the points depict the results of the Kelvin–Voigt (KV) fit of the dispersion curves obtained using the PGE method.

The phase velocity dispersion curves show that PGE method can retrieve phase velocity values for both mediums in the frequency range $f = (230, 1230)$ Hz for the elastic and $f = (110, 440)$ Hz for the viscoelastic. In this range, both methods accurately describe the theoretical KV elasticity model. Note that due to the absence of viscosity, the dispersion curve in the elastic case is almost flat. In contrast, for the viscoelastic case the phase velocity increases with increasing frequency. In addition, in the latter case the large wave attenuation damps the high-frequency components of the pulse and the cut-off frequency is reduced.

To evaluate the accuracy of the PGE method in estimating elasticity and viscosity, numerical experiments simulating both elastic and viscoelastic conditions were conducted, varying shear elastic and viscous moduli. Subsequently, KV coefficients were derived by fitting the phase velocity dispersion curves obtained via the PGE method to the KV model. The results of the phase velocity dispersion curves for each of the media under investigation can be found in the Supplementary Material 3. The resulting shear elastic and viscoelastic moduli for both elastic and viscoelastic media are depicted in Fig. 4. Overall, the fitted results exhibit a strong concordance with the theoretical values, particularly within the elastic media data set. This is evidenced by the gray line, which indicates the ideal correlation. The error for the elastic case, Fig. 4(a, b), shown in the corresponding insets, are less than 3% for the estimation of the shear elastic modulus. On the other hand, for viscoelastic media the retrieved μ_1 parameter exhibits a high degree of concordance with theoretical values across most viscosity values, see Fig. 4(c, d). In this case, the relative error for the estimation of μ_1 is around 5%. Similarly, the PGE method accurately estimates the viscous modulus for values up to 1.5 Pa s, showing a relative error for the estimation of μ_2 below 10% for moderate μ_2 values. However, for viscous media such as $\mu_2 > 1.5$ Pa s, the method yields a considerable degree of inaccuracy, amounting to approximately 20%. Analyzing the case $\mu_2 = 1.5$ Pa s at $f = 500$ Hz and $c_s = 2.5$ m/s, the shear wave absorption is given by $\alpha_s \omega^2 \approx 475$ Np/m. In this regime, exponentially attenuated waves present a decay length of 2.1 mm, smaller than the wavelength at this frequency. In fact, we can set the maximum frequency to $f_{\max} = c_s^2 \rho_0 / 2\pi\eta$. For the medium with 1.5 Pa s viscosity, this maximum frequency corresponds to about 660 Hz, which is around the frequency limit of the wave motion spectrum, see Fig. 3(i). Above this threshold, the wavelength is shorter than π times the decay length and, therefore, shear waves behave as evanescent modes, which are hardly processed by the PGE algorithm.

3.2. Simulation validation for heterogeneous medium

The ability of the proposed technique to reconstruct phase velocity maps is tested using a simulated medium that contains a cylindrical inclusion that is stiffer than the surrounding medium. As the 2D-FT method [33] cannot provide maps, we use the local phase velocity imaging (LPVI) method [21] for comparison. This method is based on the local wavenumber estimation (LWE) by the spatio-temporal Fourier transforms using block processing, and has been previously tested to image elastic and viscoelastic inclusions showing a great robustness [22]. Fig. 5 shows the performance for both techniques. First, Fig. 5(a–c) and (g–i) illustrates velocity maps for individual frequencies 800, 1000 and 1200 Hz for the PGE and LPVI method, respectively. The average velocity maps at these three frequencies (800–1200 Hz) are shown in Fig. 5(d, j). Both methods correctly reconstruct the circular shape of the inclusion, and the values of the shear wave speed. The axial and lateral cross-sections are shown in Fig. 5(e, f). It is important to note that in order to make an accurate comparison of axial and lateral resolution between methods, a block size of 2×2 mm was used in the LPVI method. This parameter must be smaller than the size of the inclusion to be evaluated, in this case 8 mm, in order to perform a satisfactory edge detection [20]. Results show that both methods provide a smooth step between the background and the inclusion, where the smoothness scale corresponds to the wavelength. Fig. 5(k) shows phase velocity dispersion curves calculated within the inclusion and for a region of interest in the background (marked in Fig. 5(d, j)). Local dispersion curves calculated using 2D-FT method are also shown for reference. Results show good agreement between methods, were PGE and LPVI methods retrieving nearly same phase velocity values for the inclusion and for the background.

3.3. Experimental validation in phantom

Experimental results using the phantom, including 10-mm diameter spherical inclusions, are summarized in Fig. 6. We present the shear wave velocity images for the four inclusions, two softer and two harder than the background, calculated by the PGE method and compared with the LPVI method. In all cases, the shear wave phase velocity images shown are obtained as the mean speed value in the corresponding bandwidth. Reconstructed velocity maps for each individual frequency of each of the inclusions can be found in the Supplementary Material 4. For the softer inclusions, Type I and II, the frequencies for compounding the final map were lower (350–550 Hz) than for stiffer inclusions, Type III and IV (415–810 Hz). The reason for this is that longer wavelengths are produced because of the slower-moving waves in soft inclusion. To preserve the same spatial resolution, lower frequency components are examined. PGE and LPVI approaches produce similar results. Some artifacts are visible for soft inclusions, Fig. 6(a,b). Note that shear wavefront is refracted inside soft spheres, which has the effect of focusing the wave inside the elastic cavity. Therefore, out-of-plane shear waves travel through the image plane, and both methods cannot estimate the 3D wavenumber components, only the projection on the image plane is retrieved. Therefore, this can result in errors during phase speed imaging. For the stiffer inclusion, this effect is opposite,

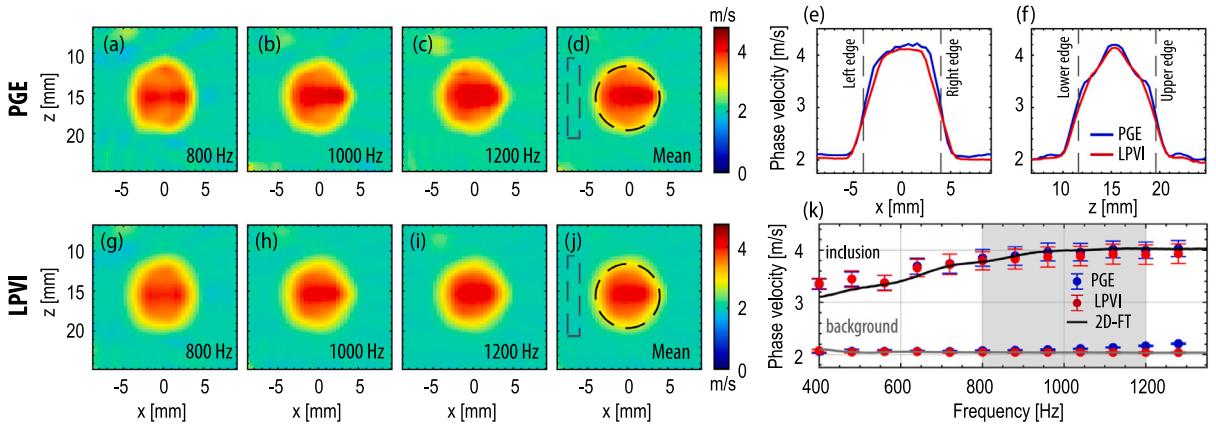


Fig. 5. Shear phase velocity maps are calculated by PGE (a–d) and LPVI method (g-d) for a mean frequency bandwidth between 800 and 1200 Hz. Lateral (e) and axial (f) profiles at the inclusion central depth are compared between PGE (blue line) and LPVI (red line), and for size reference, inclusion edges are represented by the dashed vertical lines. Phase velocity curves (k) of the background and the inclusion calculated by the PGE (blue) and LPVI (red) methods and the values obtained by the 2D-FT method are marked as reference curves in the inclusion (solid black line) and in the background (solid gray line).

and waves are refracted beyond the image plane, therefore, the images usually present an overall better quality.

Finally, Fig. 6(c,f,i,l) show phase velocity dispersion curves, respectively, measured inside each sphere and over the surrounding material. Error bars for phase velocity values obtained with the PGE and LPVI method represent the standard deviation of the averaged data within the regions of interest, shown in Fig. 6(a,b). The local phase velocity data obtained for the PGE method agrees both, LPVI and 2D-FT techniques. The design of this commercial phantom is such that elasticity is dominant over viscosity, therefore, dispersion is weak for all types of inclusions. Table 1 summarizes the retrieved shear wave velocity values at the central frequency. The value provided in the phantom datasheet, assuming an elastic and isotropic medium, is given as a reference. Note that the background curve is similar for all inclusions. The data obtained by both methods is highly correlated and, moreover, agree well in most cases with the manufacturer's values.

3.4. Experimental validation using ex vivo tissues

The results for the experimental validation using *ex vivo* tissues are shown in Fig. 7. First, Fig. 7(a,b) shows the B-mode ultrasound image and a photograph of the sample, where the morphology of the sample can be seen. However, the B-mode gray-level and speckle noise pattern in the tissue is similar than the surrounding medium, and only the edges are clearly identified. To go beyond morphology, the phase velocity maps reconstructed with PGE and LPVI methods are computed, and shown in Fig. 7(c, d), respectively. In this case, phase velocity maps were obtained by calculating the mean of the 6 maps within a frequency range spanning from 350 to 550 Hz, which allows phase velocity mapping with a resolution of 3 mm.

The phase velocity maps reconstructed with both methods reveal a circular object exhibiting higher stiffness than the surrounding medium. This is accompanied by a soft inner region at the core. In fact, this variation in elasticity is caused by the formalin pre-treatment to the *ex vivo* liver cylinder, which stiffens the edges more than the central region. A visual inspection of liver inclusion slice, shown in Fig. 7(b), reveals that the edges exhibit a darker color compared to the interior region, providing further support for the observed stiffness pattern due to the formalin pre-treatment.

The reconstructed elasticity image comprises 155×315 pixels, with lateral and axial pixel distances of $dz = 0.10$ mm and $dz = 0.05$ mm, respectively. For the LPVI method, a block size of 2.5 mm is selected to facilitate the detection of the inner hole of the inclusion.

The time required to reconstruct an image for a single frequency is 156.73 s for the LPVI 2D method and 13.58 s for the LPVI 1D method, respectively. In comparison, the PGE method requires only 0.16 s. Finally, the mean phase velocity map for the six study frequencies was calculated, requiring a total time of 935.5 and 81.48 s using the LPVI 2D and 1D method, respectively, and 0.9 s using the PGE method.

3.5. Algorithm complexity

The relationship between computation time and image size is depicted in Fig. 8 for the proposed method (blue) and the LPVI comparison method (red). Additionally, the computational times for the LPVI method are compared across its two versions: one utilizing two-dimensional Fourier transforms, LPVI-2D [20], and another, more optimized version, employing one-dimensional Fourier transforms, LPVI-1D [21]. The two versions of the LPVI method have been implemented in MATLAB, using the built-in FFT. The FFT length in both the temporal and spatial dimensions was 1024. Furthermore, it is important to highlight that the block processing of the LPVI method has been parallelized in order to enhance its computational efficiency, whereas the PGE method has not necessitated this optimization. It is essential to acknowledge that all the phase velocity maps generated in the preceding chapters of this work using the LPVI method were produced using the LPVI-2D method. Images of varying sizes, ranging from 2.5×10^3 to 120×10^3 pixels, were processed to determine computation times for both methods.

Table 1
Mean shear wave velocity and standard deviation were calculated for the four spherical inclusions and background of the phantom using the phase gradient elastography (PGE), local wavenumber approach (LPVI), and manufacturer (Ref.) methods.

Mean phase velocity (m/s)	Type I		Type II		Type III		Type IV	
	Mean ± Std	Ref.	Mean ± Std	Ref.	Mean ± Std	Ref.	Mean ± Std	Ref.
Inclusion PGE	1.42 ± 0.06	1.41	1.52 ± 0.04	1.73	3.17 ± 0.08	3.46	4.05 ± 0.18	4.83
Inclusion LPVI	1.40 ± 0.07		1.55 ± 0.04		3.23 ± 0.08		4.26 ± 0.23	
Background PGE	2.30 ± 0.06	2.45	2.39 ± 0.02	2.45	2.51 ± 0.02	2.45	2.42 ± 0.02	2.45
Background LPVI	2.32 ± 0.06		2.41 ± 0.02		2.54 ± 0.02		2.44 ± 0.02	

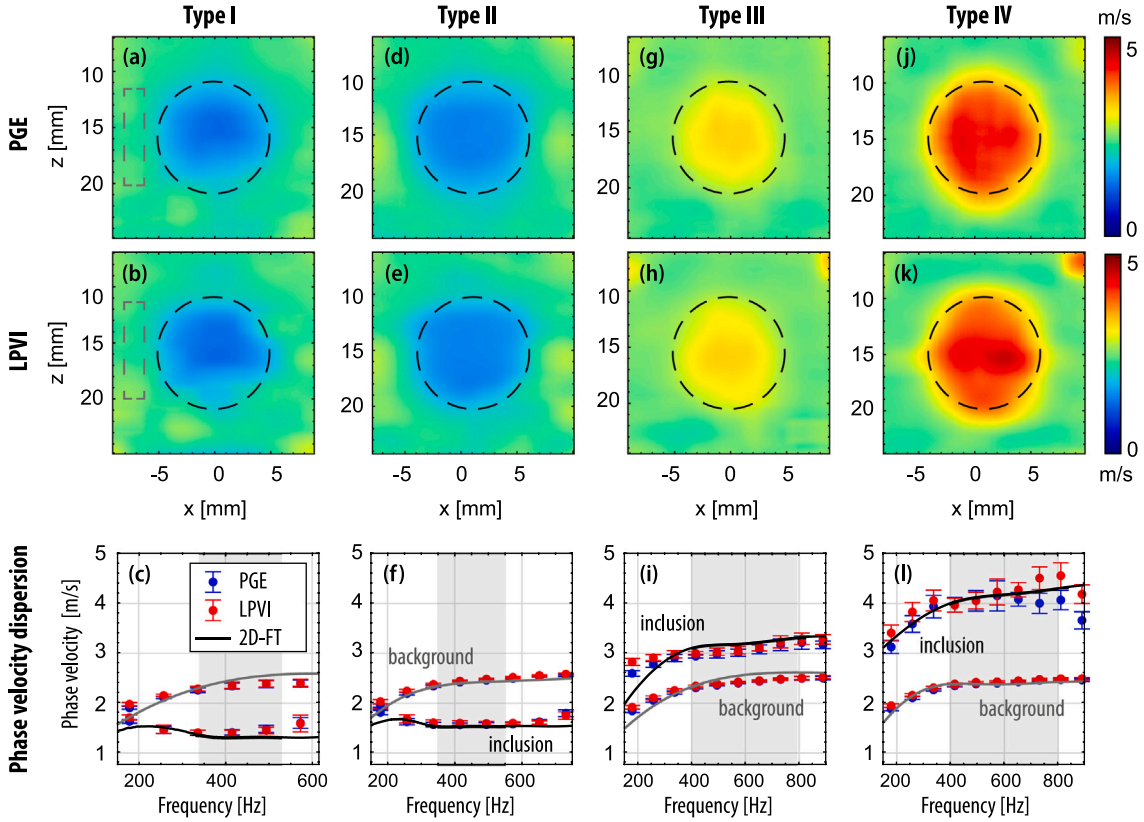


Fig. 6. Experimental shear wave phase velocity maps for the CIRS elasticity phantom. Comparison between phase gradient method (first row) and local wavenumber imaging (second row) is given for each spherical inclusion. The final row displays the phase velocity curves for the suggested technique (crosses), the computation using the local wavenumber (dots), and the 2D Fourier transform (solid line).

Table 2
Fitting parameters for the computational complexity model.

Method	$t = a \cdot n + b$	Slope
PGE	$0.4 \cdot 10^6 \cdot n + 0.1$	a_{PGE}
LPVI-1D	$266.3 \cdot 10^6 \cdot n + 0.1$	$690 \cdot a_{PGE}$
LPVI-2D	$3072.7 \cdot 10^6 \cdot n + 1.2$	$7968 \cdot a_{PGE}$

To evaluate numerical complexity, computation times were fitted to the linear expression $t = a \cdot n + b$, where n represents the number of pixels, t denotes the computation time, and a and b are constants. The results of this fitting are presented in Table 2. The data reveals that both methods exhibit linear algorithmic complexity, denoted as $\mathcal{O}(n)$. However, the slopes of the linear fits differ for each method. The LPVI method demonstrates a significantly steeper slope than the PGE method, with the LPVI slope in the LPVI-2D version being approximately 8000 times greater than that of the PGE method, and around 700 times greater in the LPVI-1D version.

4. Discussion

The results indicate that the proposed method can reconstruct phase velocity maps in soft tissues with high resolution and low computational times. Furthermore, the implementation in the frequency domain facilitates the retrieval of phase velocity dispersion and tissue viscoelasticity.

The proposed method assumes a progressive shear wavefront, i.e., a quasi-plane and unidirectional wave traveling through the medium. Consequently, a key aspect of the method is the directional bandpass filtering, which decomposes the wavefront into different directions, thereby producing a smoother wavefront that enhances phase gradient method performance. The bandwidth of the directional filter is crucial for accurately capturing the angular components of shear wave propagation in elastography. For quasi-planar waves, which predominantly travel horizontally (0° or 180°) in homogeneous media, narrow bandwidths (e.g., $\Delta\varphi = \pi/32$) are sufficient. However, in heterogeneous media where shear waves undergo diffraction or refraction, resulting in deviations from the horizontal axis, a larger bandwidth is needed to accommodate the additional angular components. Numerical simulations suggest that intermediate bandwidths ($\pi/8 \leq \Delta\varphi \leq \pi/4$) strike a balance by capturing essential wavefront details without losing spatial information, making them optimal for both homogeneous and heterogeneous media. Therefore, the choice of bandwidth should reflect the physical characteristics of the waves, particularly in heterogeneous media, to avoid phase velocity inaccuracies caused by wavefront distortions. Flatter wavefronts can be generated using high f-number for focusing the pushing beam. Further information is available in the Supplementary Material 2. Other pushing strategies as Supersonic Shear Wave Imaging [10] or Comb Push Shear Elastography [37] can also enhance method efficacy by generating a quasi-plane wavefront, but directional filtering still be needed to avoid unidirectional shear-wave propagation.

The method's capability to identify elastic and viscoelastic parameters was assessed. As viscosity increases, particularly when $\mu_2 > 1.5$ Pa s, the method's accuracy diminishes. While the KV parameters of elastic media are accurately reconstructed in all cases, in the case of extreme viscous media, the calculation of shear moduli μ_1 and μ_2 becomes less accurate, see e.g. Fig. 4(d), due to shear wave motion losses, resulting in a reduced reconstruction region near the focal zone. Experimental testing in various viscoelastic phantoms is recommended for further validation. Future work should explore additional rheological models beyond the KV model to accommodate a broader range of biological tissues.

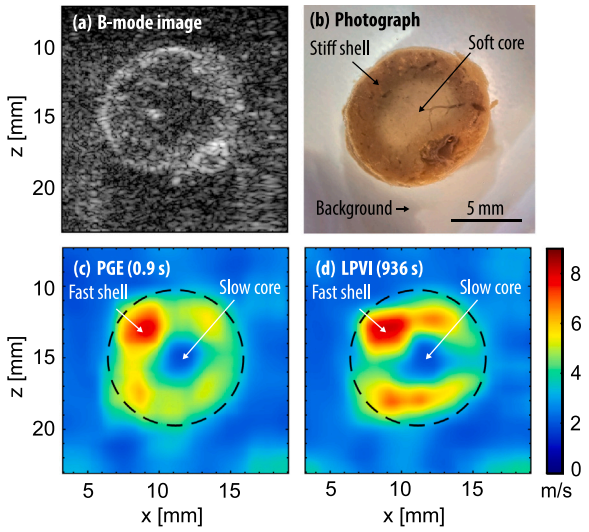


Fig. 7. (a) B-mode ultrasound image of the *ex vivo* sample, (b) Photograph of a sample slice. (c) The average phase velocity between 350 and 550 Hz of the sample for the proposed PGE method and (d) the LPVI method, displaying the different areas affected by the formalin pretreatment.

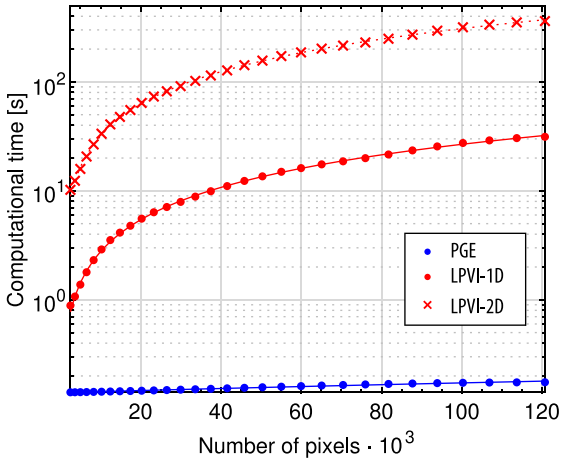


Fig. 8. Computation time is analyzed as a function of the degrees of freedom, corresponding to the total number of pixels in an image. The red and blue points represent the computation time results obtained using the local wavenumber (LPVI) and phase gradient (PGE) approaches, respectively. The LPVI method is evaluated in both its (red points) LPVI-1D and (red crosses) LPVI-2D versions. The expression $t = a \cdot n + b$ is used to fit the data (continuous lines).

Simulations (Fig. 5) and experiments (Figs. 6, 7) were used to test the approach, and the results demonstrate that the proposed method can image heterogeneous media with a good contrast ratio between the object and the surrounding medium. Notably, simulated and experimental results from phantoms with spherical inclusions reveal that reconstructing soft inclusions, such as Type I, is less accurate than reconstructing rigid spheres. This discrepancy arises because the surface of soft spheres acts as a refracting lens, focusing the shear wave front inside the sphere due to slower propagation velocity, which impacts the planar and uniform amplitude of the wavefront and restricts the measured motion field to a two-dimensional plane, neglecting out-of-plane waves. The incomplete data set leads to an incomplete reconstruction of the wavenumber, significantly affecting the phase velocity reconstruction in soft spheres compared to hard spheres.

In addition, when reconstructing a phase velocity map, the selection of the frequency range is also important. Factors to consider include the modulation of the corresponding frequency content by the medium's elastic modulus. Experimental results (Fig. 6) indicate that softer inclusions are better reconstructed within a lower frequency range (350 to 550 Hz) compared to stiffer inclusions (415 to 810 Hz). To achieve the desired spatial resolution, the frequency content must cover a broad range of wavelengths and angular spectra. The spatial resolution of the proposed method is comparable to other frequency-based techniques, utilizing shorter wavelengths at higher frequencies, which is essential for detecting small inclusions. The shear wave motion energy spectrum was used to determine the frequency range limits. The lowest frequency should ensure the longest wavelength is within the region of interest, while the maximum frequency should resolve the smallest object to be imaged.

The proposed method yields results comparable to those provided by the phantom manufacturer, with some discrepancies, particularly for the stiffest inclusion (Type IV). The values provided by the manufacturer are indicative due to various factors affecting the evaluation of elastic material properties, such as temperature, measurement technique, or frequency used. The characterization methods differ, with the manufacturer using a quasi-static uniaxial compression test and this study employing a dynamic approach. The utilization of distinct elastographic assessment techniques may imply the existence of a measurement bias that exhibits variability across different systems, as evidenced by prior research findings [38]. Consequently, the reference value offered by the manufacturer is the Young's modulus, with shear velocity values calculated assuming an isotropic elastic medium.

According to the manufacturer, this phantom is designed to be elastic; however, the dispersion curves indicate slight dispersion across all four types of inclusions (Fig. 6), with a particularly notable increase in phase velocity for phantom IV, where it escalates from 3.2 m/s at 200 Hz to approximately 4.2 m/s at 800 Hz. Dispersive behavior has been observed in elastography studies involving complex media with geometric constraints. On the one hand, guided modes, as the ones propagating in artery walls, can introduce physical frequency-dependent phase and group velocity variations [39]. On the other hand, spherical inclusions can introduce artifacts in imaging tissue stiffness, as they cause refraction and scattering of shear waves at their boundaries [40]. In our study, the spherical inclusions in the phantom likely refract the shear wavefront, producing out-of-plane wave components whose transverse wave vector component is not captured at the imaging plane, leading to an apparent dispersion in phase velocity measurements.

Finally, although all spectral the tested methods present a similar algorithmic complexity, the PGE technique significantly reduces the computational time compared to the LPVI method. For example, when reconstructing a 150 × 150-pixel image using the phase gradient approach requires a mere 0.14 s, whereas the parallelized LPVI 2D and 1D technique on a desktop computer (CPU Intel(R) Core (TM) i9-10900F CPU at 2.80 GHz and 32 GB RAM) necessitates 72.8 and 5.95 s, respectively. Additionally, for larger images, the proposed method scales almost linearly, therefore, the computational efficiency is maintained. This improvement is due to the block processing required by the LPVI method, which involves local Fourier transforms, whereas the phase gradient technique evaluates the entire image area globally by calculating the gradient in each direction using a fast estimator based on finite differences. This efficient approach opens a tentative path for fully volumetric quantitative elastography.

5. Conclusion

In this paper we presented an efficient method for soft-tissue elastography by reconstructing shear wave phase velocity maps. The imaging technique is based on the generation and tracking of shear waves by using ultrasound. Thanks to angular filtering, a simple and fast phase-gradient approach can be used to locally calculate the shear

wavenumber with a fine spatial resolution in the frequency domain. The combination of angular filtering and phase gradients provides an efficient, robust and fast method to generate elasticity maps of soft tissues. In addition, by measuring the phase-velocity dispersion, the proposed method is able to characterize both elastic and viscoelastic media.

The technique has been validated using both simulation and experimental data, using phantoms and also *ex vivo* soft tissues, demonstrating a high accuracy and a fine spatial resolution. In particular, the algorithm reveals inner structures in soft tissues which are not visible for morphological imaging methods like conventional B-mode imaging, and it quantifies its stiffness by mapping its shear wave phase velocity. These results are comparable to those provided by several benchmark spectral methods, but the present method significantly reduces the computation time, up to two or three orders of magnitude. In this way, the phase-gradient method is revealed as an efficient approach for real-time phase velocity map reconstruction.

CRediT authorship contribution statement

Enrique González-Mateo: Writing – original draft, Writing – review & editing, Visualization, Validation, Software, Methodology, Investigation, Formal analysis, Data curation, Conceptualization. **Francisco Camarena:** Funding acquisition. **Noé Jiménez:** Conceptualization, Writing – review & editing, Visualization, Validation, Supervision, Software, Resources, Project administration, Methodology, Investigation, Funding acquisition, Formal analysis.

Declaration of competing interest

The authors declare that they have no known competing financial interests or personal relationships that could have appeared to influence the work reported in this paper.

Acknowledgments

This research has been supported by the Ministerio de Ciencia, Innovación y Universidades, Spain and Agencia Estatal de Investigación, Spain grants RYC2021-034920-I, PID2022-142719OB-C21, PID2019-111436RB-C22 and CNS2023-145707 funded by MCIN/AEI/10.13039/501100011033; Agencia Valenciana de la Innovació, Spain grants INNVA2/2022/11, INNVA1/2022/37, INNVA1/2020/92, and Generalitat Valenciana, Spain grants CIAICO/2023/052 and IDIFEDER/2021/004.

Appendix A. Simulation method

For algorithm testing, shear wave motion simulations in a three-dimensional medium were performed. For this purpose, we combined semi-analytical and numerical techniques in two stages. First, we calculate the ultrasound beam emitted by the probe to push the tissue, and the corresponding acoustic radiation force. Second, an elastodynamics simulation was implemented to calculate the shear wave propagation in the soft solid.

The acoustic field of the push beam can be calculated by means of the Rayleigh-Sommerfeld Integral [41]. While this approach can describe fine geometrical details of the probe such as the kerf of the piezoelectric elements, it becomes slow to compute a volumetric set of query points. On the other hand, angular spectrum methods are efficient to project a field from a 2D transverse field, but the number of points in the transverse plane cannot usually describe fine geometrical details. Therefore, we combine both methods to avoid their limitations. First, we use the Rayleigh-Sommerfeld integral to calculate the radiated field of the transducer on a transverse 2D plane as

$$P(x,y,z_i) = \sum_{n=1}^{N} u_n \frac{i\omega\rho_0}{2\pi} \int_{S_n} \frac{e^{ik|\mathbf{r}_i-\mathbf{r}_n|}}{|\mathbf{r}_i-\mathbf{r}_n|} dS_n, \tag{A.1}$$

where $\mathbf{r}_i = (x,y,z_i)$ is the position of the transverse plane, located near the source at a depth z_i, N is the total number of piezoelectric elements, $\mathbf{r}_n(x,y,z)$, S_n, and u_n are the position, surface and normal velocity amplitude of the nth piezoelectric element, respectively, ρ_0 is the medium mass density, ω is the central frequency of the pushing beam, $k = \omega/c_p$, and c_p is the sound speed in the tissue. Once the field at the transverse plane is known, it can be projected efficiently over the entire volume, $P(x,y,z)$, using the angular spectrum method [42,43]. In the spatial Fourier space, each spectral component of the field at the transverse plane is given by

$$P\left(k'_x,k'_y,z_i\right) = \iint_{-\infty}^{+\infty} P(x,y,z_i) e^{i(k'_x x + k'_y y)} dx dy, \tag{A.2}$$

where the transverse components of the acoustic wavevector are $k'_x = k\cos\theta\sin\phi$, and $k'_y = k\sin\theta\sin\phi$, and θ, and ϕ are the azimuth, and elevation angle of each plane wave in the spectral decomposition. Each spectral component at $z = z_i$ is projected to an arbitrary distance z by multiplying it in the Fourier space with the spectral propagator $H(k'_x,k'_y,z_i,z)$ as

$$P(k'_x,k'_y,z) = P(k'_x,k'_y,z_i) H(k'_x,k'_y,z_i,z), \tag{A.3}$$

where the spectral propagator for the pressure field, assuming a Fourier time convention of the type $e^{i\omega t}$, is defined as [42],

$$H(k'_x,k'_y,z_i,z) = e^{-ik'_z|z-z_i|}, \tag{A.4}$$

where the axial component of the acoustic wavevector is given by

$$k'_z = \sqrt{k^2 - (k'^2_x + k'^2_y)}. \tag{A.5}$$

Therefore, if $k_x^2 + k_y^2 \le k^2$, then k_z is real and the propagator considers propagating modes, while if $k_x^2 + k_y^2 > k^2$, then k_z is purely imaginary and the propagation function models the rapidly decaying evanescent modes of the field. Angular restriction is applied to avoid aliasing of rapidly oscillating waves propagating at grazing angles, using a low-pass circular window of radius $k_c = k\sqrt{D^2/2(D^2/2+z^2)}$ in the k-space [43]. Finally, for each spectral component, an inverse spatial Fourier transform of $P(k_x,k_y,z)$ is computed to recover the field amplitude $P(x,y,z)$ in the spatial domain,

$$P(x,y,z) = \iint_{-\infty}^{+\infty} P\left(k_x,k_y,z\right) e^{-i(k_x x + k_y y)} dx dy. \tag{A.6}$$

Combining these two methods results in a computationally efficient approach to calculate the 3D-acoustic field of the pushing beam produced by an ultrasound imaging probe.

For shear wave propagation simulation, a pseudo-spectral time-domain simulation method was used, as implemented in the open-source k-Wave MATLAB Toolbox [44]. This method numerically solves the coupled constitutive and motion equations for an isotropic viscoelastic medium, assuming a Kelvin–Voigt (KV) model. The ARF generated by the push beam is used as a body-force input for the elastic simulation, and can be expressed in vector form as [45],

$$\mathbf{F}(x,y,z) = i\frac{\alpha_p(\omega)}{2\omega\rho_0 c_p}\left(P\cdot\nabla P^* - P^*\cdot\nabla P\right), \tag{A.7}$$

where α_p is the ultrasound absorption coefficient. On the other hand, the Kelvin–Voigt model parameters are the shear elastic modulus, $\mu_1 = c_s^2\rho_0$, and the shear viscous modulus, $\mu_2 = 2\alpha_s\rho_0 c_s^3$, where c_s and α_s are shear wave speed and shear wave absorption coefficient α_s, respectively. Recall that the phase velocity dispersion of a Kelvin–Voigt medium is given by [35]

$$c_p(\omega) = \sqrt{\frac{2\left(\mu_1^2+\omega^2\mu_2^2\right)}{\rho_0\left(\mu_1+\sqrt{\mu_1^2+\omega^2\mu_2^2}\right)}}, \tag{A.8}$$

therefore, the elastic and viscous modulus can be retrieved by fitting the phase velocity dispersion data to the model.

Appendix B. Supplementary data

Supplementary material related to this article can be found online at https://doi.org/10.1016/j.cmpb.2024.108529.

References

[1] J.H. Holmes, D.H. Howry, G.J. Posakony, C.R. Cushman, The ultrasonic visualization of soft tissue structures in the human body, Trans. Am. Clin. Climatol. Assoc. 66 (1955) 208–225.

[2] J. Ophir, I. Céspedes, H. Ponnekanti, Y. Yazdi, X. Li, Elastography: a quantitative method for imaging the elasticity of biological tissues, Ultrason. Imaging 13 (2) (1991) 111–134.

[3] K. Nightingale, S. McAleavey, G. Trahey, Shear-wave generation using acoustic radiation force: in vivo and ex vivo results, Ultrasound Med. Biol. 29 (12) (2003) 1715–1723, http://dx.doi.org/10.1016/j.ultrasmedbio.2003.08.008, publisher: Elsevier.

[4] L. Sandrin, S. Catheline, M. Tanter, X. Hennequin, M. Fink, Time-resolved pulsed elastography with ultrafast ultrasonic imaging, Ultrason. Imaging 21 (4) (1999) 259–272.

[5] T. Sugimoto, S. Ueha, K. Itoh, Tissue hardness measurement using the radiation force of focused ultrasound, in: IEEE Symposium on Ultrasonics, Vol. 3, 1990, pp. 1377–1380, http://dx.doi.org/10.1109/ULTSYM.1990.171591.

[6] L. Sandrin, M. Tanter, S. Catheline, M. Fink, Shear modulus imaging with 2-d transient elastography, IEEE Trans. Ultrason. Ferroelectr. Freq. Control 49 (4) (2002) 426–435, http://dx.doi.org/10.1109/58.996560.

[7] R.G. Barr, Z. Zhang, Shear-wave elastography of the breast: Value of a quality measure and comparison with strain elastography, Radiology 275 (1) (2015) 45–53, http://dx.doi.org/10.1148/radiol.14132404, pMID: 25426770.

[8] S. Chen, M. Fatemi, J.F. Greenleaf, Quantifying elasticity and viscosity from measurement of shear wave speed dispersion, J. Acoust. Soc. Am. 115 (6) (2004) 2781–2785.

[9] A.P. Sarvazyan, O.V. Rudenko, S.D. Swanson, J.B. Fowlkes, S.Y. Emelianov, Shear wave elasticity imaging: a new ultrasonic technology of medical diagnostics, Ultrasound Med. Biol. 24 (9) (1998) 1419–1435.

[10] J. Bercoff, M. Tanter, M. Fink, Supersonic shear imaging: a new technique for soft tissue elasticity mapping, IEEE Trans. Ultrason. Ferroelectr. Freq. Control 51 (4) (2004) 396–409.

[11] S. Catheline, J.-L. Thomas, F. Wu, M. Fink, Diffraction field of a low frequency vibrator in soft tissues using transient elastography, IEEE Trans. Ultrason. Ferroelectr. Freq. Control 46 (4) (1999) 1013–1019.

[12] C. Fang, A. Lim, P.S. Sidhu, Ultrasound-based liver elastography in the assessment of fibrosis, Clin. Radiol. 75 (11) (2020) 822–831.

[13] C. Kronlage, A. Grimm, A. Romano, J.-H. Stahl, P. Martin, N. Winter, J. Marquetand, Muscle ultrasound shear wave elastography as a non-invasive biomarker in Myotonia, Diagnostics 11 (2) (2021) 163.

[14] G. Bosio, N. Zenati, F. Destrempes, B. Chayer, G. Pernod, G. Cloutier, Shear wave elastography and quantitative ultrasound as biomarkers to characterize deep vein thrombosis in Vivo, J. Ultrasound Med. 41 (7) (2022) 1807–1816.

[15] N.C. Rouze, M.H. Wang, M.L. Palmeri, K.R. Nightingale, Robust estimation of time-of-flight shear wave speed using a radon sum transformation, IEEE Trans. Ultrason. Ferroelectr. Freq. Control 57 (12) (2010) 2662–2670.

[16] H. Zhao, P. Song, M.W. Urban, R.R. Kinnick, M. Yin, J.F. Greenleaf, S. Chen, Bias observed in time-of-flight shear wave speed measurements using radiation force of a focused ultrasound beam, Ultrasound Med. Biol. 37 (11) (2011) 1884–1892.

[17] T. Deffieux, G. Montaldo, M. Tanter, M. Fink, Shear wave spectroscopy for in vivo quantification of human soft tissues visco-elasticity, IEEE Trans. Med. Imaging 28 (3) (2009) 313–322.

[18] J. Ormachea, K.J. Parker, Reverberant shear wave phase gradients for elastography, Phys. Med. Biol. 66 (17) (2021) 175001.

[19] N. Tano, R. Koda, S. Tanigawa, N. Kamiyama, Y. Yamakoshi, M. Tabaru, Continuous shear wave elastography for liver using frame-to-frame equalization of complex amplitude, Ultrason. Imaging 46 (3) (2024) 197–206.

[20] P. Kijanka, M.W. Urban, Local phase velocity based imaging: A new technique used for ultrasound shear wave elastography, IEEE Trans. Med. Imaging 38 (4) (2019) 894–908.

[21] P. Kijanka, M.W. Urban, Fast local phase velocity-based imaging: Shear wave particle velocity and displacement motion study, IEEE Trans. Ultrason. Ferroelectr. Freq. Control 67 (3) (2020) 526–537.

[22] P. Kijanka, M.W. Urban, Local phase velocity based imaging of viscoelastic phantoms and tissues, IEEE Trans. Ultrason. Ferroelectr. Freq. Control 68 (3) (2021) 389–405.

[23] G.-Y. Li, Y. Cao, Assessing the mechanical properties of anisotropic soft tissues using guided wave elastography: Inverse method and numerical experiments, J. Acoust. Soc. Am. 142 (3) (2017) 1526–1536.

[24] E. Rizzuto, R. De Luca, A. Musarò, Z. Del Prete, Measuring and modelling nonlinear elasticity of ex vivo mouse muscles, J. Healthc. Eng. 2021 (2021) 5579232.

[25] J. Bercoff, A. Criton, C. Bacrie, J. Souquet, M. Tanter, J. Gennisson, T. Deffieux, M. Fink, V. Juhan, A. Colavolpe, D. Amy, A. Athanasiou, ShearWave™ elastography a new real time imaging mode for assessing quantitatively soft tissue viscoelasticity, in: 2008 IEEE Ultrasonics Symposium, 2008, pp. 321–324.

[26] G. Pinton, J. Dahl, G. Trahey, Rapid tracking of small displacements with ultrasound, IEEE Trans. Ultrason. Ferroelectr. Freq. Control 53 (6) (2006) 1103–1117.

[27] T. Loupas, J. Powers, R. Gill, An axial velocity estimator for ultrasound blood flow imaging, based on a full evaluation of the Doppler equation by means of a two-dimensional autocorrelation approach, IEEE Trans. Ultrason. Ferroelectr. Freq. Control 42 (4) (1995) 672–688.

[28] S.L. Lipman, N.C. Rouze, M.L. Palmeri, K.R. Nightingale, Evaluating the improvement in shear wave speed image quality using multidimensional directional filters in the presence of reflection artifacts, IEEE Trans. Ultrason. Ferroelectr. Freq. Control 63 (8) (2016) 1049–1063.

[29] A. Manduca, D.S. Lake, S.A. Kruse, R.L. Ehman, Spatio-temporal directional filtering for improved inversion of MR elastography images, Med. Image Anal. 7 (4) (2003) 465–473.

[30] P. Song, A. Manduca, H. Zhao, M.W. Urban, J.F. Greenleaf, S. Chen, Fast shear compounding using robust 2-D shear wave speed calculation and multi-directional filtering, Ultrasound Med. Biol. 40 (6) (2014) 1343–1355.

[31] H. Zhao, P. Song, D.D. Meixner, R.R. Kinnick, M.R. Callstrom, W. Sanchez, M.W. Urban, A. Manduca, J.F. Greenleaf, S. Chen, External vibration multi-directional ultrasound shearwave elastography (EVMUSE): Application in liver fibrosis staging, IEEE Trans. Med. Imaging 33 (11) (2014) 2140–2148, http://dx.doi.org/10.1109/TMI.2014.2332542, conference Name: IEEE Transactions on Medical Imaging.

[32] M.L. Palmeri, Y. Deng, N.C. Rouze, K.R. Nightingale, Dependence of shear wave spectral content on acoustic radiation force excitation duration and spatial beamwidth, in: 2014 IEEE International Ultrasonics Symposium, 2014, pp. 1105–1108.

[33] D. Alleyne, P. Cawley, A two-dimensional Fourier transform method for the measurement of propagating multimode signals, J. Acoust. Soc. Am. 89 (3) (1991) 1159–1168.

[34] B. Fornberg, Generation of finite difference formulas on arbitrarily spaced grids, Math. Comp. 51 (184) (1988) 699–706.

[35] S. Catheline, J.-L. Gennisson, G. Delon, M. Fink, R. Sinkus, S. Abouelkaram, J. Culioli, Measurement of viscoelastic properties of homogeneous soft solid using transient elastography: An inverse problem approach, J. Acoust. Soc. Am. 116 (6) (2004) 3734–3741, http://dx.doi.org/10.1121/1.1815075.

[36] J.R. Cook, R.R. Bouchard, S.Y. Emelianov, Tissue-mimicking phantoms for photoacoustic and ultrasonic imaging, Biomed. Opt. Express 2 (11) (2011) 3193–3206.

[37] P. Song, H. Zhao, A. Manduca, M.W. Urban, J.F. Greenleaf, S. Chen, Comb-push ultrasound shear elastography (CUSE): A novel method for two-dimensional shear elasticity imaging of soft tissues, IEEE Trans. Med. Imaging 31 (9) (2012) 1821–1832, http://dx.doi.org/10.1109/TMI.2012.2205586, conference Name: IEEE Transactions on Medical Imaging.

[38] J. Oudry, T. Lynch, J. Vappou, L. Sandrin, V. Miette, Comparison of four different techniques to evaluate the elastic properties of phantom in elastography: is there a gold standard? Phys. Med. Biol. 59 (19) (2014) 5775–5793.

[39] A. Caenen, M. Pernot, K.R. Nightingale, J.-U. Voigt, H.J. Vos, P. Segers, J. D'hooge, Assessing cardiac stiffness using ultrasound shear wave elastography, Phys. Med. Biol. 67 (2) (2022) 02TR01.

[40] N.C. Rouze, M.H. Wang, M.L. Palmeri, K.R. Nightingale, Parameters affecting the resolution and accuracy of 2-d quantitative shear wave images, IEEE Trans. Ultrason. Ferroelectr. Freq. Control 59 (8) (2012) 1729–1740, http://dx.doi.org/10.1109/TUFFC.2012.2377.

[41] S.M. Kirkup, Computational solution of the acoustic field surrounding a baffled panel by the Rayleigh integral method, Appl. Math. Model. 18 (7) (1994) 403–407.

[42] D.-L. Liu, R.C. Waag, Propagation and backpropagation for ultrasonic wavefront design, IEEE Trans. Ultrason. Ferroelectr. Freq. Control 44 (1) (1997) 1–13.

[43] X. Zeng, R.J. McGough, Evaluation of the angular spectrum approach for simulations of near-field pressures, J. Acoust. Soc. Am. 123 (1) (2008) 68–76.

[44] B.E. Treeby, J. Jaros, D. Rohrbach, B.T. Cox, Modelling elastic wave propagation using the k-Wave MATLAB Toolbox, in: 2014 IEEE International Ultrasonics Symposium, 2014, pp. 146–149.

[45] F. Prieur, O.A. Sapozhnikov, Modeling of the acoustic radiation force in elastography, J. Acoust. Soc. Am. 142 (2) (2017) 947–961.